This document is the Accepted Manuscript version of a Published Work that appeared in final form in ***ACS Catalysis***, copyright © 2023 American Chemical Society, after peer review and technical editing by the publisher. To access the final edited and published work see
https://pubs.acs.org/doi/10.1021/acscatal.3c00779

Available online: 5 June 2023
DOI: 10.1021/acscatal.3c00779
Cite this: ACS Catal. 2023, 13, 12, 8206–8218

This document is confidential and is proprietary to the American Chemical Society and its authors. Do not copy or disclose without written permission. If you have received this item in error, notify the sender and delete all copies.

Assessing and Quantifying Thermodynamically Concomitant Degradation during Oxygen Evolution from Water on $SrTiO_3$

Hanna Lyle,[#] Suryansh Singh,[#] Elena Magnano, Silvia Nappini, Federica Bondino, Sadegh Yazdi,[*] and Tanja Cuk[*]

ABSTRACT: The oxygen evolution reaction (OER) from water, while more stable on transition metal oxide surfaces than others, has nonetheless proved to be concomitant with charge-induced surface degradation. Since heterogeneous and nanostructured electrodes are often used and with a large excitation area, the degradation can be difficult to quantify. Here, we utilize single crystalline $SrTiO_3$, highly efficient photoexcitation of the OER, and a focused laser to spatially define the degradation. A repetitive, ultrafast laser pulse above the band gap energy is employed, which allows for highly varied exposure of the surface using different scan methods. It also connects the work to the OER and its time-resolved mechanisms. By characterizing the degradation using optical spectroscopy and electron microscopy, the material dissolution constitutes an upper bound of 6% of the charge passed in a pH 13 electrolyte, while for pH 7, it reaches 23%; the pH dependence is anticorrelated with the ultrafast population of trapped charge. Although a minority component, the remarkable consistency of the 6% upper bound in the pH 13 electrolyte across a large range of linearly increasing degradation volumes and changing electrode composition defines a dominant lattice dissolution reaction as thermodynamically concomitant with the OER. Along with the pH dependence, the elemental composition of the degraded layer quantified by energy-dispersive and photoelectron and absorption X-ray spectroscopy suggests the relevance of certain chemical cation redeposition reactions. Altogether, using spatially and temporally defined photoexcitation of a crystalline surface provides a means to quantify semiconducting transition metal oxide degradation during the OER and constricts its mechanisms.

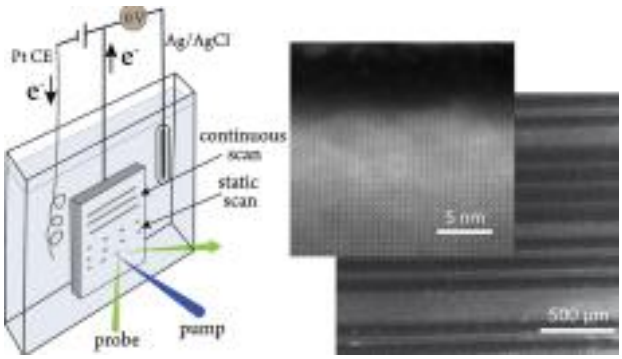

KEYWORDS: *water splitting, oxygen evolution reaction, lattice oxygen evolution reaction, degradation mechanisms, metal oxides, time-resolved spectroscopy*

INTRODUCTION

Water splitting has the potential to produce a clean, renewable, and storable energy source in H_2, and water oxidation is utilized in conjunction with CO_2 reduction for liquid fuels. Yet, the stability of many catalysts used for the oxygen evolution reaction (OER) from water is problematic for the continual and sustainable production of such fuels.

The stability can vary significantly across materials and reaction conditions. While the transition metal (TM) oxides are generally more stable than the main group compounds, their stability changes down and across the periodic table and is pH dependent. Further, small amounts of surface degradation which at the most encompassing level is “any destruction of a material under chemical or electrochemical action of the surrounding environment”, altering it from the initial one[1,2]are relevant for long-term fuel production. At electrochemical interfaces, the degradation can be purely chemical or charge-induced. For the OER, surface degradation is often discussed as having two parts:[3] dissolution of the material into the electrolyte and reconstruction of an amorphous TM oxide surface from metal cations. The degradation itself is observed by imaging (atomic force microscopy, electron microscopy), spectroscopy (X-ray photo electron spectroscopy, X-ray absorption spectroscopy, and optical spectroscopy), and elemental analysis (energy-dispersive spectroscopy) post catalysis. Some examples of degradation under anodic conditions of the OER by either voltage or light excitation include (a) $BiVO_4$ for which Bi and V dissolve into solution,[4,5] accompanied by 50−200 nm of the material, yielding an amorphous Bi−O layer,[4] (b) $Ba_{0.5}Sr_{0.5}Co_{0.8}Fe_{0.2}O_{3-\delta}$ (BSCF) for which the thickness of amorphous regions become >20 nm after >100 cycles,[6,7] (c) Sr leaching from $SrIrO_3$ and other iridates (Sr_2IrO_4, Sr_4IrO_6),[8,9] which leads Sr^{2+} to diffuse and O^{2-} to reorganize into a disordered Sr_xIrO_3 with higher Ir−O content,[8] and (d)

dissolution of rutile TiO_2 resulting also in the formation of an amorphous layer of titanium hydroxide.[10] The more active materials are less stable and, further, degradation through dissolution and reconstruction often creates a more stable surface while decreasing activity.[11]

The similarity of the degradation accompanying the OER across all of these TM oxides has suggested that common mechanisms are involved. Proposed degradation mechanisms often refer to a Pourbaix diagram,[1,12] which calculates the stability of a material with respect to applied potential and pH. Yet, the OER catalysts are found to dissolve and reconstruct in nominally stable regions of the diagram, which has been attributed to reaction kinetics associated with nearby instabilities.[13] The reaction kinetics of especially oxidizing photo-holes has been implicated, with successful surface passivation attributed to judiciously shuttling holes to the OER over degradation. Surface passivation has been achieved by controlled deposition often atomic layer deposition of thin films of TiO_2 and Al_2O_3, among others.[14−18] While the particular mechanism for shuttling holes may be different, surface passivation has also been achieved by the electro deposition of thicker metal oxide/(oxy)hydroxide overlayers of CoPi, CoO_x, or FeOOH.[19−23]

On the other hand, a thermodynamic argument has been made for TM oxide dissolution. The Pourbaix diagrams are not constructed during the OER or presume a constant partial pressure of O_2. If one utilizes chemical potentials during the reactions, the lattice oxygen, O_2^-, could already be thermodynamically unstable at the Nernstian potential of the OER by a dominant dissolution reaction.[3] This dissolution reaction is referred to as the lattice oxygen evolution reaction (LOER). For a perovskite with A and B noble metal sites, the LOER occurs by

$$ABO_3 \rightarrow BO_2 + A_{aq}^{2+} + \frac{1}{2}O_2 + 2e^- \quad (1)$$

$$BO_2 \rightarrow B_{aq}^{2n+} + \frac{n}{2}O_2 + 2ne^- \quad (2)$$

The generality of these interpretations suggests that quantifying the degradation would provide key data by which to assess whether the degradation is, in fact, thermodynami cally allowed during the OER and, if so, to what extent it competes with the OER. This work treats degradation as a product that can be directly compared to the oxygen evolution from water. The methodology utilizes a single crystalline and nominally stable TM oxide (STO: 0.1% Nb-doped $SrTiO_3$ (100)), highly efficient photoexcitation of the OER, and a spot size defined by a laser beam. The spatial definition allows a degradation volume to be associated with the charge passed through the photoexcited spot. Furthermore, the methodology utilizes different scan methods, which modulate the surface exposed to a repetitive, pulsed laser beam to achieve highly varied degradation volumes. The pulsed photoexcitation also allows for an optical probe of the excited state surface.

The surface is probed using a combination of ground and excited state optical reflectance, electron microscopy and spectroscopy, and X-ray spectroscopy. The following essential findings are made: (1) Upper bounds of the material dissolution are 6% of the total charge passed for pH 13 and 23% for pH 7 (treating both the dissolution and OER as 4- electron processes), (2) a porous TM oxide is left behind, with significant Ti and Sr having dissolved, (3) the remaining TM oxide is comprised of local SrO and TiO_2 motifs and a larger percentage of Ti and O compared to stoichiometric $SrTiO_3$, and (4) the pH dependence of the dissolution is anticorrelated with the meta-stable population of trapped holes formed within <2 ps. The remarkable consistency of the upper bound of 6% in the pH 13 electrolyte over a large range of linearly increasing degradation volume and changing electrode composition demonstrates a dominant dissolution reaction to be thermodynamically concomitant with the OER. Separately, the value reports on how competitive the LOER is with the OER for STO and the excitation conditions chosen here. Finally, the elemental composition of the degraded layer and the pH dependence suggest the relevance of certain chemical cation redeposition mechanisms. The results motivate future work utilizing these methods on varied crystal structures of titanium dioxides in a larger range of electrolytes and for other semiconducting TM oxides that drive OER photoelectrochemistry.

PHOTOELECTROCHEMISTRY OF STO, SCANNINGMETHODS, & SURFACE PROBES

The oxygen evolution reaction from water is driven by a band gap excitation of 0.1% Nb-doped $SrTiO_3$ 100 (STO) in an electrochemical cell where STO is held at a constant potential of 0 V vs Ag/AgCl for which the dark current is negligible. The STO band gap is excited with pulsed 266 nm light (400 fs, 500 Hz) that creates a photocurrent. The pump beam has an area of 4.7×10^{-4} cm^2 (Figure S1) and results in a quantum efficiency of light-to-charge separation of greater than 70% (Figure S2). The fluence is held constant at 0.04 mJ/cm^2 such that 2% of the surface sites are excited by every pump pulse. The resulting steady-state current of 2.5 mA/cm^2 for the Faradaic OER corresponds to ~1 O_2/site-sec of the illuminated area; in this calculation, all of the surface sites are presumed to contribute to oxygen evolution. Predom inantly, the data is taken at pH 13 in a 0.1 M NaOH

electrolyte. The one comparison made is to pH 7 in a 0.1 M $NaSO_4$ electrolyte. The photo-holes in the VB of the STO sit at 2.8 V vs reversible hydrogen electrode (RHE), which results in an over-potential of 1.6 V for the OER.

The STO electrode in 0.1 M NaOH is chosen for three reasons. First, it is highly selective for the OER. The current resulting from ultraviolet photoexcitation on reduced single crystals in 3-electrode configurations like ours, with ~0 V vs Ag/AgCl on the working electrode, a Pt counter electrode, and high quantum efficiency of charge separation (~100% with λ < 330 nm) has been shown to be Faradaic for the OER using mass spectrometry[24,25] and gas chromatography[26] in a NaOH electrolyte. We confirmed approximately Faradaic OER (±20%) for our configuration in 0.1 M NaOH using an O_2 sensor for excitation by a continuous Xenon lamp and a 400 fs, 500 Hz laser (albeit with significantly less accumulated charge) in previous work.[27] These measurements do not preclude minority component side reactions from the solid or the electrolyte. In the 0.1 M NaOH electrolyte, side reactions are limited to H_2O_2 formation and free $OH^{\bullet}$. Over the years, both have been found to be minority components in TiO_2;[28] while H_2O_2 is prone to decomposition, the free $OH^{\bullet}$ production, in particular, is measured by coumarin scavenging to be below 1% of the UV photoexcitation.[29] The side reactions from the solid are the topic of this work.

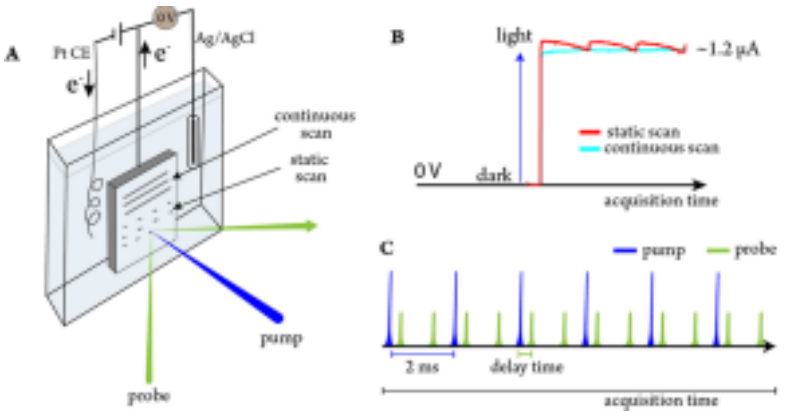

D Sample names

Sample	Electrolyte pH	Scan method
A13	13	28 μm/s
B13	13	7 μm/s
C13	13	100 s/spot
D13	13	60 min/spot
B7	7	7 μm/s

Figure 1. Experimental setup and naming scheme. (A) The cartoon of STO in the electrolytic cell at 0 V vs Ag/AgCl. The pump (266 nm, 0.04 mJ/cm^2) is normal to the sample surface, while the broadband white light probe is at a 45° angle of incidence. Panel (B) shows the increase in current from dark (no pump exposure, ~0 μA) to light on (0.04 mJ/cm^2, ~1.2 μA) for both a continuous scan (blue) and a static scan (red). (C) The cartoon shows the repetition of the pump pulses (blue) and the pump-on and pump-off shots of the probe pulses (green). Delay is the time between the pump and probe pulses in the on-shot, and acquisition time is the total time spent on the sample, comprising many pump and probe pulses. (D) The naming scheme for samples with different scan methods and electrolyte conditions.

Second, the metals are in their noble metal configurations, Ti(IV) and Sr(II), in STO. This implicates dissolution reactions in which the charge transfer is predominantly associated with oxygen sites. Further, doping by Nb leads primarily to delocalized electrons. It has been shown that electrons localized on Ti sites (*e.g.*, Ti(III)) are not detectable in the crystal prior to catalysis,[30] and those measurements are repeated here. Finally, the 100-crystal face of the STO electrode was chosen due to previous characterization of its surface termination,[30−32] OER photoelectrochemistry,[26] and most recently, transient optical reflectance during the OER.[33,34]

We now turn to the timing of the photoexcitation and the associated scanning methods. A sequence of ultrafast 266 nm, 500 Hz pump pulses arrive at the sample (Figure 1). For each data point, there is both a time to acquire from many repetitive pump pulses on the sample (acquisition time) and a time difference between the pump and the optical probe (delay time). The acquisition time is the primary metric of the degradation. The degradation is modulated by the scan method (*i.e.*, x−y−z stage motion), and there are two methods: “static scan” and “continuous scan”. In the static scan, acquisition times are acquired over multiple spots on the sample that are separated by a fixed distance. Each spot is exposed to the 266 nm pump for a fixed amount of time (*e.g.*, 100 s/spot or 50000 pump pulses within 100 s). In the continuous scan, the sample stage is moved at a fixed rate (*e.g.*, 7 or 28 μm/s) while all times are acquired sequentially. The resulting degradation patterns are represented by the cartoon in Figure 1A, while the photocurrents are shown in Figure 1B, and the sequence of pump and probe pulses is depicted in Figure 1C. Continuous scanning creates rows of degradation on the sample, while static scanning creates individual spots of degradation. The important distinction between these two methods is that by continuously scanning across the sample, each pump shot arrives on a “clean” sample surface, and so sequential time points are treated equally. On the other hand, in the static scan method, the first shot arrives on a clean surface, but each sequential shot arrives on an increasingly degraded one. Figure 1D provides a naming

scheme for the different scan conditions. The letters denote the scan method and speed; sequential letters represent increasing acquisition time from a given surface area. The numbers 7 and 13 identify the solution pH. Representative photocurrents versus acquis ition time for all of these conditions are reported in Figure S2.

The surface characterization techniques organize the rest of the manuscript. We start with the optical reflectance, which is collected both from the ground (pump off) and excited state (pump on) surfaces. The optical reflectance defines the scan methods and identifies the linearity of the degradation with acquisition time when the optical probe is sensitive enough to measure it. Next, scanning electron microscopy (SEM) and scanning transmission electron microscopy (STEM) were employed to directly observe the degraded volume and quantify the degradation with respect to the measured photocurrents. In the next section, energy-dispersive X-ray spectroscopy in STEM (EDS), X-ray photoemission spectros copy (XPS), and X-ray absorption spectroscopy (XAS) quantify the noble metal dissolution and give an approximate composition for the remaining oxide. The last section on transient optical reflectance (TR) compares the changes in the degradation between pH 7 and pH 13 to the initial concentration of trapped holes. The full list of surface characterization and abbreviations used in the manuscript are shown in Table 1. A comparable list accompanying Figure S1 orders the surface and electrochemical characterization for the Supporting Information.

OPTICAL REFLECTANCE

Figure 2 reports on the sample degradation by the ground and excited state optical reflectance, while the photocurrent evolves in a pH 13 electrolyte. Continuous scanning results in a constant photocurrent, while the static scan method results in a decreasing photocurrent during each period (Figure 2A). While the photocurrent is higher initially for the static scan, this is due to sample-to-sample variations of the exact quantum efficiency of the prepared electrode. Figure 2B shows that the ground state optical reflectance remains constant for the continuous scan while it decreases for the static scan. Given that the static scan involves a decreasing photocurrent, the decrease in reflectance can be attributed to a roughened surface that scatters the optical probe, which we return to below.

Table 1. Surface Characterization, Materials, and Reactions

Surface Characterization	
STEM	scanning transmission electron microscopy
HAADF-STEM	high-angle annular dark-field scanning transmission electron microscopy
EDS	energy-dispersive X-ray spectroscopy
AFM	atomic force microscopy
SEM	scanning electron microscopy
XPS	X-ray photoelectron spectroscopy
XAS	X-ray absorption spectroscopy
TEY	total electron yield
TR	transient optical reflectance (UV−vis)
Materials	
STO	0.1% Nb-doped $SrTiO_3$ 100
TM	transition metal
Reactions	
OER	oxygen evolution reaction
LOER	lattice oxygen evolution reaction

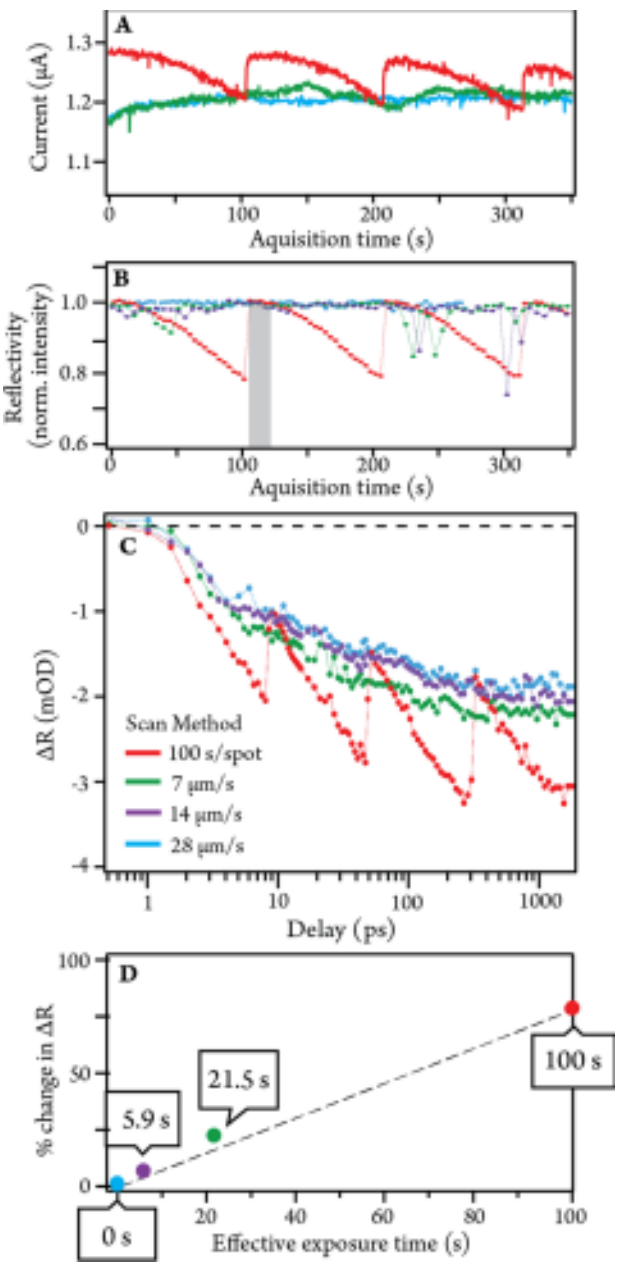

The excited state reflectance also changes while the photocurrent evolves and as a function of the scan method. Upon photoexcitation, surface-trapped holes create electronic states in the middle of the band gap, as

Figure 2. Ground and excited state optical reflectance of STO in the pH 13 electrolyte with exposure to the 266 nm pump for different scan methods (red = static scan and green, purple, and blue = continuous scans). (A) Current passing through the electrode vs acquisition time. (B) The intensity of the broadband optical probe reflected from the sample vs acquisition time. (C) Kinetic trace of ΔR from the sample at 400 nm. (D) % change in Δ*R*, with respect to the 28 μm/s signal, vs calculated effective pump exposure time (see the text and Supplementary Figure S3).

determined previously for STO.[33,35,36] These states lead to emissive transitions in the UV region (<500 nm) in the reflectance, which we probe here at 400 nm. An increasingly negative change in the reflectance from the ground state (ΔR) identifies a larger hole-trapped population. However, ΔR also changes with the scan method, as shown in Figure 2C. By continuously scanning at faster speeds, the acquisition time from a given surface area decreases, and interestingly, the data converge to an unchanging ΔR. This is shown by measuring ΔR for scan speeds from 7 μm/s (green trace) to 14 μm/s (purple trace) and finally to 28 μm/s (blue trace). While the ΔR is plotted as a function of delay time, appropriate for monitoring the excited state, each increase in scan speed represents acquisition times that are indeed a factor of two shorter for an exposed surface area. This is described in Figure S3. For the static scan of 100 s/spot (red trace), each time the pump moves to a clean surface, ΔR quickly jumps to the same value as ΔR for the 28 μm/s continuous scan, then gradually decreases as the acquisition time from the same sample spot increases, only to quickly jump back to the converged signal each time the pump is moved to a clean surface. Therefore, ΔR from the 28 μm/s scan is identified as that of the nominally clean surface, with negligible contribution from the degradation.

We now turn to the sensitivity of the optical experiments and the origin of the convergence in ΔR with decreasing acquisition time. Optical reflectivity is only so sensitive to surface changes since it can probe the sample bulk. This is clearly seen in the ground state optical reflectance (Figure 2B), for which the optical reflectance change of the 100 s/spot scan with respect to the continuous scans increases linearly but only past an acquisition time of ~20 s (gray bar). Excited state data from ΔR would be more sensitive to changes at the surface due to the differential recorded for each data point, but a nonlinearity is nonetheless evident in the convergence of the continuous scans. In the following, we determine a minimum acquisition time for which changes due to the degradation are seen in the optical reflectance and beyond that they occur linearly with acquisition time. To do so, an effective exposure time is defined as the amount the sample had to be exposed to the beam to achieve a certain ΔR. Approximate linearity of ΔR with acquisition time for the 100 s/spot scan (Figure S3) is used to determine the time needed to achieve the difference between ΔR (or % change in ΔR) in the 7 and 14 μm/s scans with respect to the 28 μm/s scan. As shown in Figure 2D, the effective exposure times are 5.9 and 21.5 s, respectively, for the two scans; the 28 μm/s scan effective exposure is 0 s.

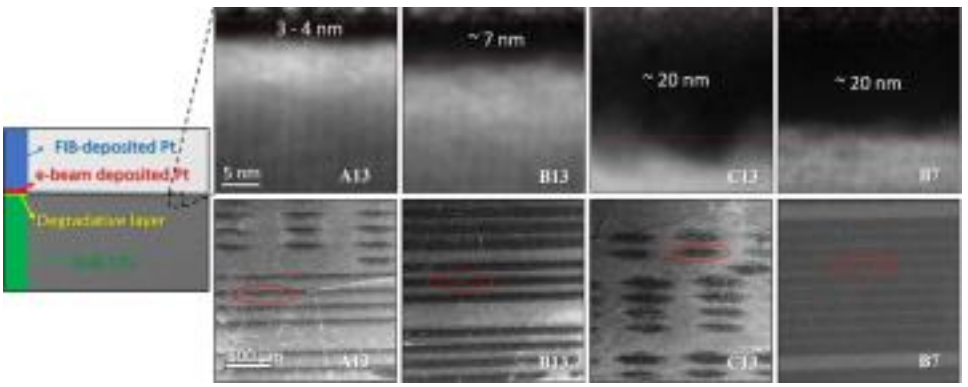

Figure 3. Electron imaging of the degraded layer. (top) STEM images of the cross-sections of samples after 266 nm pump exposure for samples A13−C13, comparing a static scan to two continuous scans at different scan speeds. B7 has the same continuous scan rate as B13 but in a pH 7 electrolyte. The bright band at the top of the STEM images (above the upper dotted red line) is the protective platinum layer deposited during sample preparation. The black band in the center shows degradation depth contrasted against the bulk (crystal structure below the lower dotted red line). To the left of the images, a cross-sectional cartoon of the degradated layer within the full sample cross-section. (bottom) SEM images for the same conditions show the degraded surface area. The red ovals mark the place from which cross-sectional STEM specimens are prepared. Dark, oval spots on the sample surface result from static scanning, whereas continuous scanning produces evenly spaced lines.

Given the assumption of linearity for the 100 s/spot scan, the % ΔR is linear with effective exposure time. However, these changes do not occur linearly with acquisition time: the 14 μm/s should be twice as fast as 7 μm/s but has an effective exposure time ~3.6 times shorter. This suggests that for the 14 μm/s scan, we are already in a nonlinear regime. Altogether, the nonlinearity in the optical reflectance below 20 s (Figure 2B), the association of this nonlinearity also in ΔR for continuous scans with exposure times <20 s (Figure 2D), and the approximate linearity of the ΔR in the 100 s/spot scan (Figures 2C, S3) identify that our experiments are insensitive to the degradation below ~20 s acquisition time and subsequently, a linear sensitivity is observed. The fact that the 28 μm/s scan optically represents a nominally clean surface is also seen directly by optical microscopy (Figure S4). The darkened lines of the 7 μm/s scans are absent in the 28 μm/s scans.

Finally, we propose a mechanism by which increasing emission (Figure 2C) occurs due to a degraded surface.

Namely, the degraded surface causes the probe to scatter, such that we collect less light through the lenses, the spectrometer, and onto the detector. ΔR is calculated as $-\log(I_{ON}/I_{OFF})$, where I_{ON} and I_{OFF} are the intensities of the probe beam with the pump on and off, respectively. For an intrinsic pump− probe ΔR from a nominally clean sample that is emissive ($I_{ON}/ I_{OFF} > 0$), where I_{ON} is a sum of I_{OFF} and the increase in probe light due to emission ($+\Delta I$), a decrease in counts for the I_{OFF} probe would cause an apparent increase in emission to be observed with increasing acquisition time. Further, for a linear decrease of the ground state reflectance, a linear increase in the degradation-induced ΔR should be observed.

ELECTRON MICROSCOPY

To connect the changes in reflectivity to degradation, the surface and depth of the photoexcited area were analyzed by SEM and cross-sectional STEM (Figure 3). The cartoon on the left shows the cross-section of the degraded layer imaged using STEM. The cross-sectional sample was prepared by the *in-situ* lift-out method in a focused ion beam microscope. The Pt layers on top of the degraded area were deposited by electron and ion beam deposition methods prior to ion milling for protection purposes. Since the sampled area by STEM is smaller than the degraded area, the surface flatness across the pristine to the degraded region was confirmed by AFM (Figure S5).

The pristine and photoexcited areas are clearly distinguish able in (secondary electron) SEM images. The degraded areas are darker than the pristine, crystalline areas. For the continuous scans of linear velocity (A13, B13), even and continuous lines are observed, while for the static scan (C13), the degradation is confined to finite area spots, such that the SEM images in Figure 3 (bottom row) reflect the cartoon of Figure 1. These observations show that we only need to consider photo-induced degradation. The degraded area for the static scan is measured directly from the photoexcited spot in the SEM images. For the continuous scans, the horizontal diameter of the photoexcited spot is set to the beam size. Since continuous lines of degradation appear in the SEM images, this diameter is arbitrary but should be consistent in the % dissolution calculations below. The depth of degradation is determined from cross-sectional STEM images shown in Figure 3 (top row) by measuring the thickness of the darkest layer between the Pt and sample bulk. All of the sample conditions, each with a full set of SEM and STEM images at different magnifications, are shown in Supplementary Figure S6.

Samples A13, B13, and C13 compare the degradation for a static scan and two different continuous scan speeds in a pH 13 electrolyte. The 28 μm/s continuous scan (A13) represents the ideal case, for which sequential pump and probe pulses incident on the surface are equivalent according to the ground and excited state optical reflectance. However, while we are insensitive to it in optical experiments, STEM shows that a thin degradation layer of 3−4 nm exists (Figure 3, top left) even for A13. Increasing surface exposure to the pump causes additional degradation. In the pH 13 electrolyte, the 7 μm/s continuous scan (B13) and the 100 s/spot static scan (C13) result in degradation depths of 7 and 20 nm, respectively. Considering the degradation depth in the ideal 28 μm/s case as a subtracted “background”, this is a 4.7× increase. The effective exposure times for B13 and C13 (21.5 and 100 s, respectively, Figure 2D) give a 4.7× increase equivalently. So, the degradation is

Table 2. Calculated Contribution of Material Dissolution to the Total Charge Passed[a]

sample	A13	B13	B7	C13	D13
STEM depth (nm) (±1 nm)	3−4	7	20	20	106
SEM area (mm^2) (±0.01 mm^2)	0.024	0.035	0.059	0.022	0.106
charge passed ($\times 10^{-5}$ C)	2.1 ± 0.038	8.6 ± 0.074	8.3 ± 0.064	12.5 ± 0.40	260
# of O-atoms from sample/2 ($\times 10^{13}$)	0.21 ± 0.10	0.6 ± 0.20	2.95 ± 0.50	1.1 ± 0.50	28 ± 2.5
O_2 from current ($\times 10^{13}$)	3.3 ± 0.059	13.4 ± 0.11	13 ± 0.10	20 ± 0.63	406
% **dissolution:** ratio of O_2 from degraded layer to O_2 from current	**6.4 ± 3.1**	**4.5 ± 1.5**	**23 ± 3.9**	**5.6 ± 2.5**	**6.9 ± 0.6**

[a]All samples are measured at 0 V vs Ag/AgCl with 266 nm pump excitation. Row 1 labels the samples by the different scan methods and electrolyte conditions, as described in Figure 1. Row 2 is the measured thickness of degradation from STEM; Row 3 is the measured surface area of degradation from SEM. Row 4 is the total charge passed through the circuit, calculated by integrating the electrochemical current over the acquisition time. Row 5 is 1/2 of the oxygen atoms present in the degradation volume, based on the oxygen-site density of STO. Row 6 is the number of O_2 molecules that evolved from the electrochemical current using 4 e^-/O_2. Finally, Row 7 is % dissolution, or the ratio of O_2 from the degradation volume to that from the current with Faradaic OER.

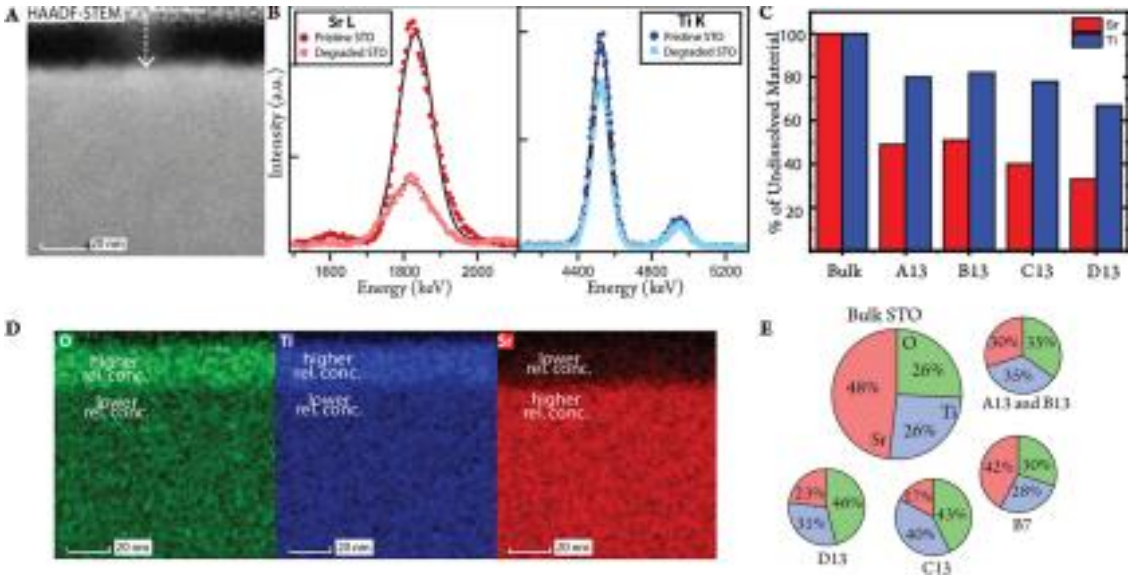

Figure 4. Chemical composition of the degraded region compared to bulk STO, measured by STEM-EDS. (A) The low magnification HAADF image of sample C13 (static scanning at 100 s/spot in the pH 13 electrolyte) showing significantly lower material density in the degraded region than bulk STO. The white dotted arrow indicates the measured depth of degradation. (B) Representative EDS Sr-L and Ti-K peaks from degraded and pristine STO regions showing significant Sr loss and relatively less Ti loss. (C) Bar graph showing the percentage of undissolved Sr (red) and Ti (blue) in the degraded region for different samples compared to bulk STO. (D) EDS weight fraction map of O, Ti, and Sr corresponding to the HAADF image in (A), showing an increase in O and Ti concentrations and a decrease in the Sr concentration in the degraded layer compared to bulk STO. (E) Pie charts show the relative weight percent of each element in the degraded volume for each sample condition alongside that of bulk STO.

linear with acquisition time, at least within the region of linearity defined by ΔR; we return to this below.

Next, we utilize the depth and areal data from the STEM and SEM images to determine the degraded volume (Table 2). A ratio of O_2 that could have arisen from this degraded volume to O_2 from the Faradaic OER then quantifies an upper limit to the dissolution reaction. For example, for the static scan C13, the measured depth (20 nm) and area (0.022 mm^2) give a degraded volume of 0.44×10^{-6} mm^2. The total number of oxygen atoms present in that volume is based on the oxygen site density in STO (5×10^{22} cm^{-3}), which for C13 is 2.2×10^{13} oxygen atoms or 1.1×10^{13} O_2 molecules. The Faradaic O_2 that could have evolved from the total current is obtained by integrating the photocurrent over the acquisition time, 100 s, which for C13 gives 12.5×10^{-5} C of charge passed and 19.6×10^{13} O_2 molecules (4 e^- per O_2). For the continuous scans, the horizontal diameter of the photoexcited spot used to determine the area from the SEM images is the same as that used to derive an acquisition time from the scan speed.

The fact that the area of degradation (0.022 mm^2) is smaller than the full width at half-maximum (FWHM) spot area of the beam (0.047 mm^2) supports using the SEM and STEM data to calculate the degradation volume. It shows that we do not have significant diffusion outside of the excitation area. Further, the areal difference likely arises from a uniform excitation area for catalysis in the center of the beam without much influence of the unexcited edges. The same is true for the rest of the conditions; the pH 7 electrolyte does have a larger degradation area, but only by ~0.01 mm^2.

Table 2 shows the dissolution percentage calculated with error bars for the different sample conditions. The error bar is ±1 nm on the STEM thickness since the AFM line profile from the pristine to the degraded region is flat to well within 1 nm (Figure S5). The error bar is ±0.01 mm^2 on the SEM area based on the resolution of the images. The error on the charge passed comes from the standard deviation in the photocurrent, which is calculated using all points collected over the acquisition time appropriate for the degradation volume and for ~5 representative sample areas to get a cumulative standard deviation (Figure S2); since the exact photocurrent for the 1 h spot (D13) was used, there is no error reported. Table S1−S3 goes through this procedure in greater detail, along with explanations for error propagation. For A13, B13, and C13, the dissolution percentages are 6.4 ± 3.1, 4.5 ± 1.5, and 5.6 ± 2.5%, respectively.

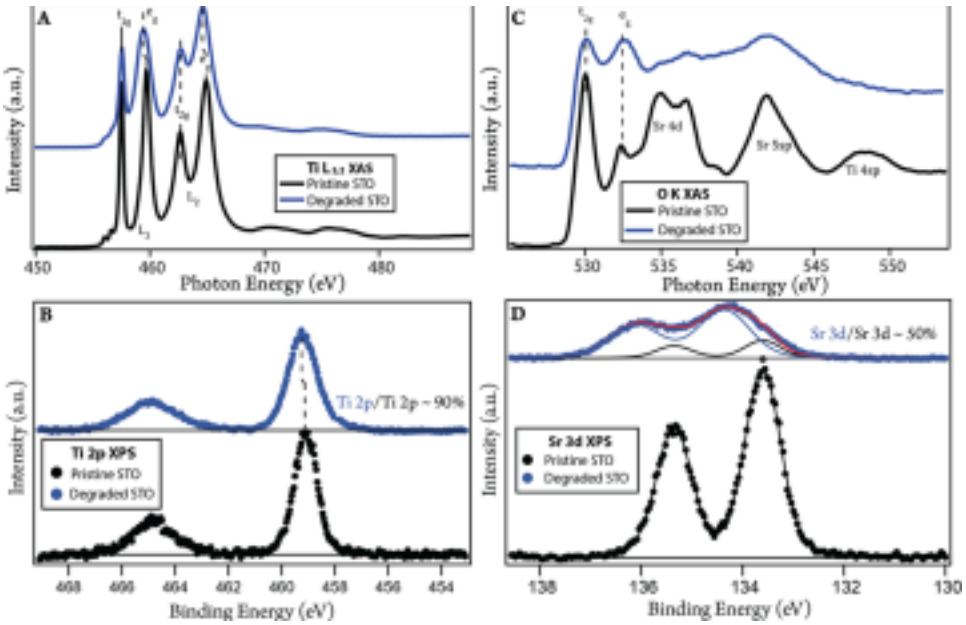

Figure 5. XAS and XPS spectra measured on pristine STO (black curves) and degraded STO after laser exposure for C13 (blue curves). (A) Ti $L_{3,2}$ XAS spectra: after exposure, while the spectra show overall O_h symmetry, the e_g peaks shift to lower photon energy, which can be explained by a distortion of the symmetry locally. (B) XPS Ti 2p core-level spectra: after exposure, the Ti 2p levels also show a shift to lower photon energy, and the spectral areal intensity decreases to ~90% of pristine STO. (C) O K XAS spectra: the spectrum measured after exposure shows a decrease in the intensity of the unoccupied O 2p orbitals hybridized with Sr 4d and Sr 5sp in agreement with the observed decrease of Sr at the surface. It also shows a similar relative intensity of the Ti t_{2g} and e_g peaks, which is explained by overlapping peaks related to local SrO_x separate from TiO_2, as described in the text. (D) XPS Sr 3d core levels: after exposure, the intensity of the Sr 3d signal at the surface decreases to ~50% of pristine STO, and the peak shape changes. The best curve fit (red line), following a previous procedure (see the text), is obtained by adding a new component shifted by ~0.9 eV from the Sr 3d pristine STO peaks explained by the formation of SrO_x. Figure S11 details the spectral intensity decrease reported in panels B and D.

The above calculations assume that the dissolution is linear with acquisition time. There are several ways this linear relationship is shown by the data: (a) the continuity of the degradation lines with a linear scan velocity, (b) linearity in the optical reflectance past the ~20 s acquisition time, (c) past ~20 s, the degradation observed by imaging increases linearly with the exposure time determined by ΔR (the 4.7× factor described above), (d) in STEM images, degradation occurs even for the fastest 28 μm/s scan, and (e) the calculation results in the same % dissolution within the error bars for the same reaction conditions (pH 13), but highly varied degradation volumes (A13, B13, C13).

We now turn to sample D13 (Figure S7), which is the hour long static scan. Here, the photocurrent decays over long periods of time, which is traditionally utilized as one of the first indicators of degradation during the OER. The largest decay occurs in the first half hour and then levels off, like other metal oxides[10,13] (Figure S2). Somewhat surprisingly, but in line with the analysis thus far, even for an hour on the spot, the contribution of the dissolution to the charge passed is 6.9 ± 0.7%, which is again within error, the same as for the rest of the scan methods at the same reaction conditions. Thus, the dissolution is a constant percentage of the total charge passed through the area, independently of whether the charge is passed through a single spot or across the entirety of the surface and, further, for how long.

ELEMENTAL COMPOSITION OF THE DEGRADED LAYER

Thus far, the surface degradation has been treated as occurring entirely due to the dissolution of the TM oxide electrode into the electrolyte from the degradation volume. While this does give a quantifiable % dissolution, an amorphous layer separate from the bulk is observed. The amorphous layer could arise from the reconstruction of the metal oxide that has not yet dissolved or from cation redeposition reactions from the electrolyte. In this section, we detail the elemental composition of this layer using EDS, XPS, and XAS of the electrode post catalysis.

Figure 4 represents the results of elemental analysis by electron spectroscopy (the full data set is shown in Figure S7). First, Figure 4A presents a typical high-angle annular dark-field (HAADF) image of sample C13, in which the degraded layer appears darker than the STO substrate. Because the HAADF signal is roughly

proportional to $Z^{1.8}$, where Z is the atomic number, the lower intensity in the degraded layer suggests that its density is significantly lower than the STO substrate. EDS analysis confirms that the lower density is due to the loss of material. By comparing the intensity of Sr-L and Ti-K EDS peaks of the bulk to the degraded region, we can determine the total dissolution of Sr and Ti from the degradation volume. Figure 4B shows these peaks for C13, while they are shown for the full sample set in Figures S8 and S9. The dissolution calculation is done by integrating the peak fits. Across the different conditions, approximately 55% of Sr and 20−30% of Ti dissolves into the solution. The percentage of undissolved Ti and Sr for A13−D13 are reported by the bar graph in Figure 4C.

Figure 4D presents the EDS weight fraction map of O, Ti, and Sr, calculated from the EDS intensity using the Cliff− Lorimer ratio technique with *k*-factors measured directly from bulk STO (see the Supporting Information for detail). These weight fraction maps, in which the elemental concentrations add up to unity at each point regardless of the material density, show an increase in O and Ti concentrations and a decrease in Sr concentration in the degraded layer compared to bulk STO. The degraded layer has a lower density due to the dissolution of Sr, Ti, and O, but this new amorphous material has a higher Ti and O concentration and a lower Sr concentration relative to stoichiometric $SrTiO_3$. These relative percentages vary across the sample conditions, as reported by the pie charts in Figure 4E. Generally, the faster the acquisition (A13 and B13 compared to C13 and D13) and the lower the pH (B7 compared to B13), the closer the degraded material is to the bulk stoichiometry.

The degraded layer was also analyzed by XPS and XAS for sample C13. To denote the degraded layer, spectra were taken crossing from the pristine surface to the degraded region using Sr 3d XPS, as detailed in Figure S10. We first discuss the titanium core-level data shown in Figure 5A and B. In Figure 5A, the Ti L-edge XAS measured in the pristine area (black curve) shows the characteristic lineshape for a perovskite $SrTiO_3$ with the intensity of the e_g peak similar to the t_{2g} peak and no bifurcation of the e_g peak characteristic of rutile and anatase TiO_2.[37] The Ti e_g peak shifts to lower photon energy in the spectrum collected from the degraded area (blue curve), but the Ti L-edge maintains the overall lineshape characteristic of octahedral cages. The XAS data is taken in total electron yield (TEY) mode. Previous papers on transition metals and rare earth elements report values less than 5 nm for the surface sensitivity of TEY, as described by ref 38 and references therein, definitely smaller than the thickness of the degraded region.[38] The XPS Ti 2p spectrum also exhibits a core-level shift, as reported in Figure 5B; the similar shift probed by XPS, which is surface sensitive to within ∼1 nm, also identifies the XAS Ti L-edge to probe the degraded layer. The core-level shift can be ascribed to a change in the chemical environment surrounding Ti atoms. A similar shift of the Ti 2p XPS was previously seen in annealed TiO_2 samples and assigned to a locally distorted O_h symmetry with a higher oxidation state of the Ti.[39] A corresponding one in the e_g peaks of Ti L-edge XAS on $SrTiO_3$ has likewise been associated with octahedral distortions related to defects.[40] Therefore, the Ti XAS and XPS data together identify local TiO_2 that maintains the octahedral cage of the perovskite, albeit a distorted one.

We now turn to the core-level data from oxygen and strontium. The XAS O K-edge of the pristine sample in Figure 5C (black curve) is dominated by the following features, as labeled by the metal orbitals with increasing photon energy. The first two peaks correspond to transitions from O 1s to Ti 3d (t_{2g})-O 2p and Ti 3d (e_g)-O 2p hybridized orbitals, respectively. The next bifurcated peak and the final two peaks correspond to transitions from O 1s to Sr 4d-O 2p, to Sr 5sp-O 2p, and to Ti 4sp-O 2p hybridized orbitals, respectively.[41] The XAS O K-edge of the degraded layer (blue curve) is markedly different from pristine STO,[42] with the Ti t_{2g} and e_g peaks of a similar magnitude and a much reduced contribution from Sr 4d and Sr 5sp. Since about 50% of the Sr dissolves, while significantly less Ti dissolves and, further, in the perovskite, O is 2:1 for Ti and 1:1 for Sr, we should see a reduced contribution of Sr in the O K-edge XAS. However, the fact that the Ti t_{2g} and e_g peaks are of similar magnitude cannot be explained by Sr dissolution alone. Previous XAS data shows that the main peak of the O K-edge of SrO_x is located at the same photon energy as the O 1s to Ti 3d (e_g)-O 2p transition of TiO_2, which would explain the similar magnitude.[43] On the other hand, the O 1s to Sr 4d-O 2p and O 1s to Sr 5sp-O 2p transitions of SrO_x would remain reduced compared to STO since they are not overlapping with any Ti-related features. Therefore, the O K-edge of the degraded layer is consistent with a composite of separate TiO_2 and SrO_x local structures, albeit with a higher TiO_2 content. Lastly, XPS Sr 3d spectra in Figure 5D show that the primary contributions to the degraded layer (blue curve) are Sr 3d peaks at 0.9 eV higher binding energy than for pristine STO (black curve). Assigned previously and especially for Sr defects within $SrTiO_3$,[44,45] this shift conclusively identifies the formation of local SrO separate from TiO_2. The XPS data for Ti 2p and Sr 3d shown in Figure 5B and D were also utilized to corroborate the Ti and Sr dissolution seen by EDS. Finding a ratio of the integrated peak area in the degraded region to the pristine surface gives a value for the undissolved percentage, which is approximately 50% for Sr and 90% for Ti. The analysis for several spots is shown in Figure S11. The dissolution percentages of Sr and Ti from XPS data are in line with the ones calculated from EDS data for the C13 sample (undissolved: 40% Sr, 80% Ti), even if discrepancies in the obtained numbers can be noticed. A possible reason for the underestimation of the dissolved atomic percentages in XPS analysis is the lower density of the degradative layer with respect to the pristine STO that can be translated into an increase of the mean free path of the photoelectrons emitted from the degraded layer and consequently a higher probed volume.

The XPS Ti 2p data were also analyzed for the presence of Ti(III), as shown in Figure S12. On the pristine surface, no Ti(III) is observed, even in resonant XPS. Further, XPS and resonant XPS together quantify a minimal contribution within the degraded area (<3%). So, while oxygen dissolves and could leave some vacancies behind, Ti(III) remains a minority species.

TRANSIENT OPTICAL REFLECTANCE AND PH DEPENDENCE

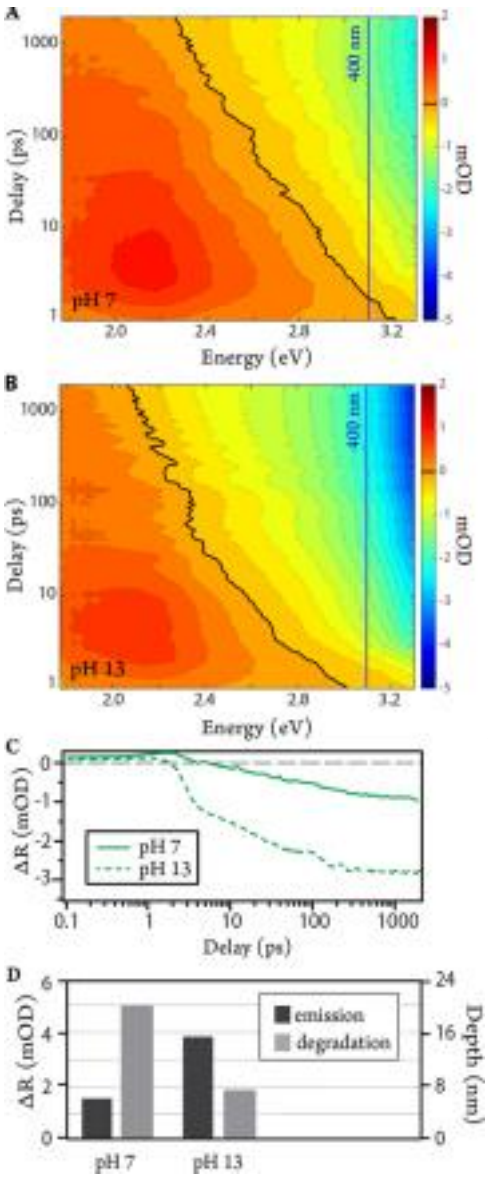

Figure 6. Excited state reflectance for STO at 0 V vs Ag/AgCl. (A) and (B) show transient reflectance (ΔR) contour plots for pH 7 and pH 13 electrolytes. The *y*-axis is the pump−probe delay time, and the *x*-axis is the spectrally resolved white light probe. Red optical density (10^{-3} OD) is positive ΔR, representing absorption, while blue optical density is negative ΔR, representing emission. The black contour lines are of zero optical density. Vertical blue lines are the kinetic traces at 3.1 eV (400 nm) shown in (C), which emphasizes the difference in the magnitude of emission between STO in basic (pH 13, dotted green) and neutral (pH 7, solid green) electrolytes. (D) Compares integrated emission from the kinetic curves (left axis) with the STEM-measured degradation depth (right axis) for each electrolyte condition.

We now address the pH 7 conditions for which a clear change in the dissolution percentage from pH 13 is observed. For the same scan method, identical calculations give 23 ± 3.9% at pH 7 (B7) as compared to 4.5 ± 1.5% (B13) at pH 13 (Table 1, Tables S1−S3). In the following, visible broadband TR is utilized to identify correlations between (a) the degradation and our converged, emissive kinetics and (b) the pH dependence of the dissolution percentage and that of the trapped hole population. The first objective builds upon previous work to further assign the emissive signal to trapped holes rather than degradation for fast enough scans, but now by directly imaging the degradation. The second objective informs on potential degradation mechanisms and their timescales, motivating future work on more detailed pH dependencies.

Figure 6A and B shows TR of the surface at pH 7 and pH 13 using a broadband optical probe (1.8−3.3 eV) through a nanosecond. As shown in detail previously, the absorptive (red) transition is not pH dependent in this time range, while the emissive (blue) transition is highly pH dependent.[33] Further, the pH dependence arises from the emissive population created <2 ps;[33,46] there is another rise in the emissive population around ∼60 ps, but this is not pH dependent. The hole-trapped population is associated with Ti−OH* or a proton and electron transfer from a surface absorbed site. The assignment derives from a precise time constant (1.3 ps) for its formation corroborated by vibrational (THz, mid-IR) spectroscopy[35,47] and the increasing emission with pH. Finally, the pH dependence shown here at the two end points can be tracked continuously with pH, resulting in a Langmuir reaction isotherm.[33] Nonetheless, we now test this assignment directly from the point of view of surface degradation, which also results in an emissive optical signal. In Figure 6C, kinetic traces at 400 nm for pH 7 and pH 13 are extracted such that they can be compared with the data in Figure 2 and Table 1. The broadband optical data were taken with the 7 μm/s scan rate to minimize degradation but also allow for efficient sample use. While the ΔR for pH 13 is a factor of 2−3 larger than for pH 7, the same data taking results in 5×'s less degradation at pH 13 (4.5%) than at pH 7 (23%) (Table 2). Therefore, for fast enough continuous scans, the pH-dependent, emissive ΔR is anticorrelated with the pH-dependent surface degradation. The anticorrelation of the emission with the degradation is depicted in the bar graph of Figure 6D, for which the STEM measured depth is plotted next to the integrated emissive signal of the kinetic traces. Thus, by utilizing short enough acquisition times, we minimize the emissive signal due to degradation and converge to the kinetics of the Ti−OH* population. Given this assessment, the imaging and transient reflectance data together imply that there is also an anticorrelation between the total trapped hole, Ti−OH* population, and the extent of surface degradation. Often, the amount of charge created at the surface per unit timeeither through shorter laser pulses with higher peak power or higher fluence for a given laser pulse is associated with more degradation. For the pH-dependent data, the same photoexcitation fluence (0.04 mJ/cm^2) was maintained, and it resulted in a similar total charge passed through the spot (Table 2, B13 and B7). Given that the total charge passed was constant,

anticorrelation between the Ti−OH* population and the surface degradation would imply that a larger population of trapped charge created at early times (<2 ps) is not concomitant with more degradation. There are two possible explanations. One is that the % dissolution is too small to be observed separately from the total trapped charge. The other is that the degradation occurs at much longer timescales. The transient spectroscopy does give a view of the meta-stability of the Ti−OH* population, which reports on how long the pH dependence of this population is anticorrelated with the % surface dissolution. The trapped hole, Ti−OH* population, is stable through a nanosecond, as shown here (Figure 6A,B), and through a microsecond, as shown previously.[34] One consistent view of the data is that a small % of charge branches off for degradation past a microsecond, while the reaction steps of the OER occur prior.

DISCUSSION

The electron imaging (STEM, SEM) and optical reflectance (ground and excited states) show that a portion of STO dissolves into the electrolyte, which consumes an upper limit of 6% of the total charge passed at pH 13 and 23% at pH 7. The dissolution reaction is explicitly charge-induced, rather than chemical, since the electron imaging clearly separates the laser beam-induced damage from the bare electrode/electrolyte contact. It also occurs concomitantly with the photo electrochemical OER from water since the dissolution comprises a minority of the photocurrent and other side reactions are minimized for STO in the NaOH electrolyte. The degradation occurs linearly with acquisition time or time exposed to the pump beam. A similar percent dissolution occurs whether the photocurrent arises from new areas of the electrode continually exposed, the same excitation spot, and whether for seconds or hours. The elemental analysis (EDS, XPS, XAS) shows explicitly that Sr and Ti dissolve into the electrolyte and that the remaining electrode material has an amorphous structure of local TiO_2 distorted octahedra, local SrO_x, and higher concentrations of Ti and O relative to the bulk. In the following, we explain these results using first a LOER dissolution reaction and second A-site and B-site cation redeposition reactions, which are consistent with the degraded electrode material. The discussion concentrates on the pH 13 condition but addresses potential mechanisms for pH depend ence.

These reactions have been proposed by several studies of surface degradation of metal oxides during the OER. We follow here the reactions and arguments within ref 3 that provides a general context for the dissolution and reconstruction of TM oxide electrodes during the OER.[3] Further, the specific delineation of reactions there applies to TM oxides without a change in the oxidation state of the metal, appropriate for “noble” transition metals Ti(IV) and Sr(II) within STO.

A lattice oxygen evolution reaction (LOER) that dissolves the electrode can arise from the instability of the oxygen anion in the TM oxide lattice. To summarize the argument, the chemical potentials within the LOER are not independent of the OER, which derives an over-potential for the LOER that is larger than or equal to the OER. While many oxides are found to be stable at OER potentials by Pourbaix diagrams, these diagrams presume that O_2 is not evolving or, more explicitly, the oxygen partial pressure is always in equilibrium. For a perovskite with A and B noble metal sites, the LOER occurs by reactions 1 and 2 in the introduction.

For STO, the A-site is the dissolution of the 2+ cation, Sr^{2+}, and the B-site is the dissolution of the 4+ cation, Ti^{4+}. Thus, reactions 1 and 2 mean that for every oxygen in the $SrTiO_3$ lattice, 1/2 O_2 and 2 e^- are released in the LOER, such that 1/ 2 O_2 arises from the Sr dissolution and one O_2 arises from the Ti dissolution. Equivalently, 4 e^- are consumed for each O_2 released, which was utilized to calculate the percent dissolution in Table 2. Since the total degradation volume was utilized for the calculation, and the electrode material does remain, this percentage represents an upper limit.

Overall, the reactions are appropriate since the material from the electrode is dissolved, and electrons occupy the oxygen orbital valence band within the electronic structure of STO. However, further, more detailed assessments from the data can be made. Common chemical potentials within the LOER and the OER are the underlying thermodynamic argument for dissolution during the OER. If so, then the amount of dissolution compared to the photocurrent should depend on the type of TM oxide and the over-potential at a particular reaction condition but should be independent of details such as the history of the electrode exposure and for how long the reactions occur. Indeed, the experiment maintains a constant current density (2.5 mA/cm^2) across all samples by the same fluence (0.04 mJ/cm^2), quantum efficiency (>70%), and applied potential (0 V vs Ag/AgCl), which demonstrates a consistent over-potential for photo-holes, whether at the nominal VB edge (2.8 V vs RHE) or a shifted one. Then, at a given pH, we obtain the same percent dissolution, regardless of whether a continuous or static scan method was employed and for highly varied acquisition times. Conversely, had kinetic processes from the electrolyte or electrode been decisive for the amount dissolved, different % dissolutions would have been obtained as the electrode evolves into an amorphous structure. This is especially anticipated for the hour spot for which the current degrades substantially (by ∼50%) and a thick 100 nm layer forms, and yet, the percentage of the total current that goes toward dissolution remains, within error, the same. The linearity of the degradation with acquisition time translates to a large range of linearly increasing degradation volumes across which we obtain a remarkably consistent % dissolution, such that the product (the degradation volume) evolves continuously as anticipated for a thermodynamically driven reaction. Another way to say this is that for a

given over potential for the OER at a particular reaction condition, the competition between the OER and the LOER is the same regardless of the history of the electrode. As such, we can really think of the chemical potential of the reactants within both as defining two concurrent reactions and, further, one dominant dissolution reaction that competes with the OER.

The LOER should be considered separate from recon structed phases in Pourbaix diagrams. For STO, there are several stable phases as a function of potential and pH. At the potential of the nominal VB that drives the OER with photo holes (1.6 V over-potential for the OER) and for pH > 7, the stable phase predicted is a reconstructed one with 3 monolayers of TiO_2 and inclusive of O* intermediates.[12] While this phase may be achieved by a concurrent reaction, the same % dissolution despite the history of the electrode means that one dominant dissolution reaction (*e.g.*, LOER) defines the degradation layer volume. We note that rutile TiO_2 is similarly nominally stable in Pourbaix diagrams over a large range potential-pH range but also exhibits degradation.[4]

A way to further test these conclusions is to apply the same methodology to other facets of STO and to the diversity of crystal geometries within titanium dioxides, which would modulate the ease with which O_2 is extracted by the LOER from a similar electronic structure. It would also be important to apply the methodology to other TM oxides, which modulate the hybridization of oxygen with the metal site. Interestingly, a degradation volume of 20−100 nm is also found after electrochemical cycling on the OER electrode BaSrCoFeO (BSCF82), and a similar procedure was utilized to estimate the contribution to charge passed.[7] While this suggests that non noble semiconducting TM oxides could be subject to a form of the LOER, an important distinction is that the metallic TM oxides in later rows of the periodic table (*e.g.*, RuO_2 and IrO_2) have proven more stable under electrochemical cycling.[48]

We next turn to the cation redeposition reactions, which can cause the appearance of an amorphous metal oxide within the degradation volume. The AFM line profiles show that while the electrode has dissolved into the electrolyte, another porous material has filled the volume up to essentially the same level as the initial surface. The elemental analysis by EDS shows that while we definitively lose Sr (~50%) and Ti (~20−30%) to the electrolyte, the relative ratios of the elements in the remaining amorphous metal oxide are lower for Sr, and higher for Ti and O compared to stoichiometric $SrTiO_3$.

We consider two simplified cation redeposition reactions. One is the cation redeposition reaction for the B-site of the perovskite

$$TiO_2 \rightarrow Ti^{4+}_{LOER} \rightarrow TiO_2 \qquad (3)$$

Since this cycle does not involve any electrons other than that evolving the O_2 to create Ti^{4+}, the redeposition would be entirely chemical and could be described, in basic conditions, by

$$Ti^{4+}_{LOER} + 4OH^- \rightarrow TiO_2 + 2H_2O \qquad (4)$$

The Ti cation redeposition reaction is further supported by the XAS and XPS data in the following way: a TiO_2 local structure separate from STO is seen by the distorted O_h environment of the Ti L-edge XAS and Ti 2p XPS. Furthermore, the resonant XPS and XPS together show that while Ti(III) is present, it is a minority species (<3%) and therefore electron transfers are not prominent in the redeposition.

A possible cation redeposition mechanism for the A-site of the perovskite is

$$Sr^{2+}_{LOER} + 2OH^- \rightarrow SrO + H_2O \qquad (5)$$

This cation redeposition reaction is further supported by XPS data of the Sr 3d core levels that distinctly show the formation of local SrO. The composite O K-edge XAS of local TiO_2 and SrO supports both cation redeposition reactions.

The extent to which both redeposition reactions take place at pH 13 can be assessed from the Ti and Sr elemental dissolution. With a total of 70−80% undissolved Ti by EDS (~90% by XPS), the Ti cations are either redeposited or did not leave. With a total of 50% undissolved Sr by EDS and XPS, 50% of the Sr cations are either redeposited or did not leave. Given that there is an amorphous TM oxide, the redeposition reactions are expected at least to compete with the LOER dissolution reaction. Given that more Sr is dissolved than Ti, we anticipate the B-cation redeposition reaction to be more effective, as has been suggested previously (CoO_x and BaSrFeCoO).[6,7] The preferential redeposition of the B-cation is also consistent with a higher O content in the amorphous metal oxide since more O redeposits with Ti than Sr.

On the other hand, at pH 7, the relative elemental percentages from the EDS weight ratios show that the remaining material is closer to the stoichiometry of bulk STO. Given the basic conditions required for both cation redeposition reactions and a preference for B-cation redeposition, repopulating TiO_2 within the degradative volume would be more efficient at pH 13 than pH 7. We also observe a larger degradation volume at lower pH, which would suggest that the cation redeposition reactions compete with the LOER to limit the dissolution at higher pH. However, an under standing of these mechanisms would require a more detailed pH dependence and the exploration of acidic pH, both of which motivate future work.

Though they naturally explain a local octahedral TiO_2 separate from SrO_x, these redeposition reactions are certainly simplified. Indeed, surface reconstructions predicted by Pourbaix diagrams could also lead to higher Ti and O content at higher pH.[12] It is also possible that excess O−O bonds are formed in a variety of configurations with Ti and Sr cations, though the dominant octahedral environment is preserved. Another possible reaction includes the formation of oxy hydroxides,[4] with additional O and H within SrO and TiO_2. Further, the exact elemental composition of the degraded layer does seem to depend on the scan method, with less change from the bulk stoichiometry for lower acquisition times. The redeposition reactions will occur concomitantly with the LOER, which changes the reactant Ti^{4+} concentration near the electrode dynamically and likely in ways that do depend on diffusive processes and electrode morphology.

Finally, we address future work that could take advantage of the quantification of the dissolution observed here. While the competition between the LOER and the OER is the same for the different sample conditions at a given pH, the OER is favored. The question is whether we can understand the favorable kinetics and then control them to reduce the degradation further. Multiscale and multiphysics models of main group semiconductors have been employed to define photostability as a percentage of the current going to the OER over degradation, which is the same as our metric here;[49] the models are carried out as a function of surface potential and charge transfer rate. With the experimental conditions and the metrics given here, the same analyses could be applied to TM oxides. Passivation methods for degradative photo-holes rely on another material accepting the holes that would otherwise go to degradation and, in certain cases, shuttling them to the OER instead.[13−22] Here, the transient spectroscopy shows that the total trapped charge going to either the OER or the LOER is anticorrelated with the percent dissolution through pH, which in and of itself suggests that there are multifaceted pathways for controlling the degradative holes. Another proposition based particularly on the use of an ultrafast repetitive laser is to modulate the timing of the laser pulses to alter when and how much charge reaches the surface.

CONCLUSIONS

By utilizing spatially and temporally defined photoexcitation of a single-crystal surface, STO, the work quantifies a dominant electrode dissolution reaction (represented by LOER) to be thermodynamically concomitant with the OER but nonethe less a minority component. The competition between the LOER and the OER is set by the over-potential of the electrode and independent of the history of the electrode exposure to the OER, as demonstrated by a remarkably consistent % dissolution despite linearly increasing degradation volumes and a changing electrode composition. Such a finding motivates future studies on whether this degradation mechanism is general for early transition metal, semiconduct ing oxides. Cation redeposition mechanisms, chemical in nature, are identified primarily by the elemental analysis of the remaining porous and amorphous TM oxide and the pH dependent degradation. The quantification of the electrode dissolution reaction by an upper bound that is anticorrelated with the total surface-trapped charge also suggests that avenues to further suppress the degradation exist.

ASSOCIATED CONTENT

* Supporting Information

The Supporting Information is available free of charge at https://pubs.acs.org/doi/10.1021/acscatal.3c00779.

Experimental setup for pump beam and scan methods; electrochemical current for all sample conditions; calculation of effective exposure time; optical, STEM, SEM, and AFM images of continuous and static scans; calculation of upper bound to % dissolution; STEM EDS of the elemental composition of degraded regions and calculation of % dissolution of Ti and Sr; XPS of Sr 3d; XPS calculation of % dissolution of Ti and Sr; XPS and resonant XPS of Ti 2p across a static scan; and details on experimental methods for electrochemical, optical spectroscopy, electron imaging, and X-ray techniques (PDF)

AUTHOR INFORMATION

Corresponding Authors
Sadegh Yazdi − *Materials Science and Engineering Program, University of Colorado, Boulder, Colorado 80303, United States; Renewable and Sustainable Energy Institute, University of Colorado, Boulder, Colorado 80303, United States;* orcid.org/0000-0002-3470-9398; Email: sadegh.yazdi@colorado.edu
Tanja Cuk − *Materials Science and Engineering Program, University of Colorado, Boulder, Colorado 80303, United States; Renewable and Sustainable Energy Institute, University of Colorado, Boulder, Colorado 80303, United States; Chemistry Department, University of Colorado, Boulder, Colorado 80309, United States;* orcid.org/0000- 0002-1635-2946; Email: Tanja.Cuk@colorado.edu

Authors
Hanna Lyle − *Materials Science and Engineering Program, University of Colorado, Boulder, Colorado 80303, United States*
Suryansh Singh − *Materials Science and Engineering Program, University of Colorado, Boulder, Colorado 80303, United States*
Elena Magnano − *IOM-CNR, 34149 Basovizza, Trieste, Italy; Department of Physics, University of Johannesburg, Auckland Park 2006, South Africa;* orcid.org/0000- 0001-6465-807X
Silvia Nappini − *IOM-CNR, 34149 Basovizza, Trieste, Italy;* orcid.org/0000-0002-4944-5487
Federica Bondino − *IOM-CNR, 34149 Basovizza, Trieste, Italy;* orcid.org/0000-0001-6505-9319

Complete contact information is available at:
https://pubs.acs.org/10.1021/acscatal.3c00779

Author Contributions # H.L. and S.S. contributed equally to the work.

Notes
The authors declare no competing financial interest.

ACKNOWLEDGMENTS

This work was supported by the Director, Office of Science, Office of Basic Energy Sciences, and by the Division of Chemical Sciences, Geosciences and Biosciences of the U.S. Department of Energy at RASEI (Boulder, CO) under Contract No. DE-SC0018939. The authors acknowledge the Facility for Electron Microscopy of Materials at the University of Colorado at Boulder (CU FEMM, RRID: SCR_019306) for providing access to electron microscopy. The authors also acknowledge Elettra Sincrotrone Trieste for providing access to its synchrotron radiation facilities. The EUROFEL project (RoadMap Esfri) funded the characterization of the samples at Elettra.

REFERENCES

(1) Pourbaix, M. *Lectures on Electrochemical Corrosion*; Plenum Press: New York-London, 1973.
(2) Hu, S.; Lewis, N. S.; Ager, J. W.; Yang, J.; McKone, J. R.; Strandwitz, N. C. Thin-Film Materials for the Protection of Semiconducting Photoelectrodes in Solar-Fuel Generators. *J. Phys. Chem. C* 2015, *119*, 24201−24228.
(3) Binninger, T.; Mohamed, R.; Waltar, K.; Fabbri, E.; Levecque, P.; Kötz, R.; Schmidt, T. J. Thermodynamic explanation of the universal correlation between oxygen evolution activity and corrosion of oxide catalysts. *Sci. Rep.* 2015, *5*, No. 12167.
(4) Eichhorn, J.; Liu, G. J.; Toma, F. M. Degradation of Semiconductor Electrodes in Photoelectrochemical Devices: Princi ples and Case Studies. In *Integrated Solar Fuel Generators*; Sharp, I. D.; Atwater, H. A.; Lewerenz, H. J., Eds.; The Royal Society of Chemistry, 2019; Vol. *22*, pp 281−303.
(5) Venugopal, A.; Kas, R.; Hau, K.; Smith, W. A. Operando Infrared Spectroscopy Reveals the Dynamic Nature of Semiconductor Electrolyte Interface in Multinary Metal Oxide Photoelectrodes. *J. Am. Chem. Soc.* 2021, *143*, 18581−18591.
(6) May, K. J.; Carlton, C. E.; Stoerzinger, K. A.; Risch, M.; Suntivich, J.; Lee, Y. L.; Grimaud, A.; Shao-Horn, Y. Influence of Oxygen Evolution during Water Oxidation on the Surface of Perovskite Oxide Catalysts. *J. Phys. Chem. Lett.* 2012, *3*, 3264−3270.
(7) Risch, M.; Grimaud, A.; May, K. J.; Stoerzinger, K. A.; Chen, T. J.; Mansour, A. N.; Shao-Horn, Y. Structural Changes of Cobalt-Based Perovskites upon Water Oxidation Investigated by EXAFS. *J. Phys. Chem. C* 2013, *117*, 8628−8635.

(8) Wan, G.; Freeland, J. W.; Kloppenburg, J.; Petretto, G.; Nelson, J. N.; Kuo, D. Y.; Sun, C. J.; Wen, J. G.; Diulus, J. T.; Herman, G. S.; Dong, Y. Q.; Kou, R. H.; Sun, J. Y.; Chen, S.; Shen, K. M.; Schlom, D. G.; Rignanese, G. M.; Hautier, G.; Fong, D. D.; Feng, Z. X.; Zhou, H.; Suntivich, J. Amorphization mechanism of SrIrO3 electrocatalyst: How oxygen redox initiates ionic diffusion and structural reorganiza tion. *Sci. Adv.* 2021, *7*, No. eabc7323.
(9) Strickler, A. L.; Higgins, D.; Jaramillo, T. F. Crystalline Strontium Iridate Particle Catalysts for Enhanced Oxygen Evolution in Acid. *ACS Appl. Energy Mater.* 2019, *2*, 5490−5498.
(10) Yang, Y.; Ling, Y.; Wang, G.; Liu, T.; Wang, F.; Zhai, T.; Tong, Y.; Li, Y. Photohole Induced Corrosion of Titanium Dioxide: Mechanism and Solutions. *Nano Lett.* 2015, *15*, 7051−7057.
(11) Danilovic, N.; Subbaraman, R.; Chang, K. C.; Chang, S. H.; Kang, Y. J.; Snyder, J.; Paulikas, A. P.; Strmcnik, D.; Kim, Y. T.; Myers, D.; Stamenkovic, V. R.; Markovic, N. M. Activity-Stability Trends for the Oxygen Evolution Reaction on Monometallic Oxides in Acidic Environments. *J. Phys. Chem. Lett.* 2014, *5*, 2474−2478.
(12) Xiong, Y.; Dabo, I. Influence of surface restructuring on the activity of SrTiO3 photoelectrodes for photocatalytic hydrogen reduction. *Phys. Rev. Mater.* 2019, *3*, No. 065801.
(13) Toma, F. M.; Cooper, J. K.; Kunzelmann, V.; McDowell, M. T.; Yu, J.; Larson, D. M.; Borys, N. J.; Abelyan, C.; Beeman, J. W.; Yu, K. M.; Yang, J. H.; Chen, L.; Shaner, M. R.; Spurgeon, J.; Houle, F. A.; Persson, K. A.; Sharp, I. D. Mechanistic insights into chemical and photochemical transformations of bismuth vanadate photoanodes. *Nat. Commun.* 2016, *7*, No. 12012.
(14) Wang, T.; Luo, Z.; Li, C.; Gong, J. Controllable fabrication of nanostructured materials for photoelectrochemical water splitting via atomic layer deposition. *Chem. Soc. Rev.* 2014, *43*, 7469−7484.
(15) Tran-Phu, T.; Chen, H.; Daiyan, R.; Chatti, M.; Liu, B.; Amal, R.; Liu, Y.; Macfarlane, D. R.; Simonov, A. N.; Tricoli, A. Nanoscale TiO2 Coatings Improve the Stability of an Earth-Abundant Cobalt Oxide Catalyst during Acidic Water Oxidation. *ACS Appl. Mater. Interfaces* 2022, *14*, 33130−33140.
(16) Moehl, T.; Suh, J.; Sévery, L.; Wick-Joliat, R.; Tilley, S. D. Investigation of (Leaky) ALD TiO2 Protection Layers for Water Splitting Photoelectrodes. *ACS Appl. Mater. Interfaces* 2017, *9*, 43614−43622.
(17) Kim, W.; Tachikawa, T.; Monllor-Satoca, D.; Kim, H.-i.; Majima, T.; Choi, W. Promoting water photooxidation on transparent WO3 thin films using an alumina overlayer. *Energy Environ. Sci.* 2013, *6*, 3732−3739.
(18) Sivagurunathan, A. T.; Adhikari, S.; Kim, D.-H. Strategies and implications of atomic layer deposition in photoelectrochemical water splitting: Recent advances and prospects. *Nano Energy* 2021, *83*, No. 105802. (19) Abdi, F. F.; Han, L.; Smets, A. H. M.; Zeman, M.; Dam, B.; van de Krol, R. Efficient solar water splitting by enhanced charge separation in a bismuth vanadate-silicon tandem photoelectrode. *Nat. Commun.* 2013, *4*, No. 2195.
(20) Seabold, J. A.; Choi, K.-S. Efficient and Stable Photo-Oxidation of Water by a Bismuth Vanadate Photoanode Coupled with an Iron Oxyhydroxide Oxygen Evolution Catalyst. *J. Am. Chem. Soc.* 2012, *134*, 2186−2192.
(21) Laskowski, F. A. L.; Nellist, M. R.; Qiu, J.; Boettcher, S. W. Metal Oxide/(oxy)hydroxide Overlayers as Hole Collectors and Oxygen-Evolution Catalysts on Water-Splitting Photoanodes. *J. Am. Chem. Soc.* 2019, *141*, 1394−1405.
(22) Nellist, M. R.; Qiu, J.; Laskowski, F. A. L.; Toma, F. M.; Boettcher, S. W. Potential-Sensing Electrochemical AFM Shows CoPi as a Hole Collector and Oxygen Evolution Catalyst on BiVO4 Water Splitting Photoanodes. *ACS Energy Lett.* 2018, *3*, 2286−2291.
(23) Shen, M.; Kaufman, A. J.; Huang, J.; Price, C.; Boettcher, S. W. Nanoscale Measurements of Charge Transfer at Cocatalyst/Semi conductor Interfaces in BiVO4 Particle Photocatalysts. *Nano Lett.* 2022, *22*, 9493−9499.
(24) Wrighton, M. S.; Ellis, A. B.; Wolczanski, P. T.; Morse, D. L.; Abrahamson, H. B.; Ginley, D. S. Strontium titanate photoelectrodes. Efficient photoassisted electrolysis of water at zero applied potential. *J. Am. Chem. Soc.* 1976, *98*, 2774−2779.
(25) Wrighton, M. S.; Wolczanski, P. T.; Ellis, A. B. Photo electrolysis of water by irradiation of platinized n-type semiconducting metal oxides. *J. Solid State Chem.* 1977, *22*, 17−29.
(26) Watanabe, T.; Fujishima, A.; Honda, K.-i. Photoelectrochemical Reactions at SrTiO3 Single Crystal Electrode. *Bull. Chem. Soc. Jpn.* 1976, *49*, 355−358.
(27) Aschaffenburg, D. J.; Chen, X.; Cuk, T. Faradaic oxygen evolution from SrTiO3 under nano- and femto-second pulsed light excitation. *Chem. Commun.* 2017, *53*, 7254−7257.
(28) Nosaka, Y. Water Photo-Oxidation over TiO2 History and Reaction Mechanism. *Catalysts* 2022, *12*, 1557.
(29) Zhang, J.; Nosaka, Y. Quantitative Detection of OH Radicals for Investigating the Reaction Mechanism of Various Visible-Light TiO2 Photocatalysts in Aqueous Suspension. *J. Phys. Chem. C* 2013, *117*, 1383−1391.
(30) Chambers, S. A.; Droubay, T. C.; Capan, C.; Sun, G. Y. Unintentional F doping of SrTiO3(001) etched in HF acid-structure and electronic properties. *Surf. Sci.* 2012, *606*, 554−558.
(31) Hussain, H.; Torrelles, X.; Rajput, P.; Nicotra, M.; Thornton, G.; Zegenhagen, J. A Quantitative Structural Investigation of the 0.1 wt % Nb−SrTiO3(001)/H2O Interface. *J. Phys. Chem. C* 2014, *118*, 10980−10988.
(32) Kawasaki, M.; Takahashi, K.; Maeda, T.; Tsuchiya, R.; Shinohara, M.; Ishiyama, O.; Yonezawa, T.; Yoshimoto, M.; Koinuma, H. Atomic Control of the SrTiO3 Crystal Surface. *Science* 1994, *266*, 1540−1542.
(33) Vinogradov, I.; Singh, S.; Lyle, H.; Paolino, M.; Mandal, A.; Rossmeisl, J.; Cuk, T. Free energy difference to create the M-OH* intermediate of the oxygen evolution reaction by time-resolved optical spectroscopy. *Nat. Mater.* 2022, *21*, 88−94.
(34) Chen, X.; Aschaffenburg, D. J.; Cuk, T. Selecting between two transition states by which water oxidation intermediates decay on an oxide surface. *Nat. Catal.* 2019, *2*, 820−827.
(35) Singh, S.; Lyle, H.; D'Amario, L.; Magnano, E.; Vinogradov, I.; Cuk, T. Coherent Acoustic Interferometry during the Photodriven Oxygen Evolution Reaction Associates Strain Fields with the Reactive Oxygen Intermediate (Ti−OH*). *J. Am. Chem. Soc.* 2021, *143*, 15984−15997.
(36) Lyle, H.; Singh, S.; Paolino, M.; Vinogradov, I.; Cuk, T. The electron-transfer intermediates of the oxygen evolution reaction (OER) as polarons by in situ spectroscopy. *Phys. Chem. Chem. Phys.* 2021, *23*, 24984−25002.

(37) Krüger, P. Multichannel multiple scattering calculation of L2,3- edge spectra of TiO2 and SrTiO3: Importance of multiplet coupling
and band structure. *Phys. Rev. B: Condens. Matter Mater. Phys.* 2010, *81*, No. 125121.
(38) Ruosi, A.; Raisch, C.; Verna, A.; Werner, R.; Davidson, B. A.; Fujii, J.; Kleiner, R.; Koelle, D. Electron sampling depth and saturation effects in perovskite films investigated by soft x-ray absorption spectroscopy. *Phys. Rev. B: Condens. Matter Mater. Phys.* 2014, *90*, No. 125120.
(39) Matouk, Z.; Islam, M.; Gutierrez, M.; Pireaux, J.-J.; Achour, A. X-ray Photoelectron Spectroscopy (XPS) Analysis of Ultrafine Au Nanoparticles Supported over Reactively Sputtered TiO2 Films. *Nanomaterials* 2022, *12*, 3692.
(40) Lobacheva, O.; Chavarha, M.; Yiu, Y. M.; Sham, T. K.; Goncharova, L. V. The local structure and ferromagnetism in Fe implanted SrTiO3 single crystals. *J. Appl. Phys.* 2014, *116*, No. 013901.
(41) Bhogra, A.; Masarrat, A.; Meena, R.; Hasina, D.; Bala, M.; Dong, C.-L.; Chen, C.-L.; Som, T.; Kumar, A.; Kandasami, A. Tuning the Electrical and Thermoelectric Properties of N Ion Implanted SrTiO3 Thin Films and Their Conduction Mechanisms. *Sci. Rep.* 2019, *9*, No. 14486.
(42) Palina, N.; Annadi, A.; Asmara, T. C.; Diao, C.; Yu, X.; Breese, M. B. H.; Venkatesan, T.; Ariando; Rusydi, A. Electronic defect states at the LaAlO3/SrTiO3 heterointerface revealed by O K-edge X-ray absorption spectroscopy. *Phys. Chem. Chem. Phys.* 2016, *18*, 13844− 13851.
(43) Nakai, S.-i.; Mitsuishi, T.; Sugawara, H.; Maezawa, H.; Matsukawa, T.; Mitani, S.; Yamasaki, K.; Fujikawa, T. Oxygen K x ray-absorption near-edge structure of alkaline-earth-metal and 3d transition-metal oxides. *Phys. Rev. B: Condens. Matter Mater. Phys.* 1987, *36*, 9241−9246.
(44) Bachelet, R.; Sánchez, F.; Palomares, F. J.; Ocal, C.; Fontcuberta, J. Atomically flat SrO-terminated SrTiO3(001) sub strate. *Appl. Phys. Lett.* 2009, *95*, No. 141915.
(45) Yoo, H. K.; Schwarz, D.; Ulstrup, S.; Kim, W.; Jozwiak, C.; Bostwick, A.; Noh, T. W.; Rotenberg, E.; Chang, Y. J. Direct visualization and control of SrOx segregation on semiconducting Nb doped SrTiO3 (100) surface. *J. Korean Phys. Soc.* 2022, *80*, 1042− 1047.
(46) Chen, X.; Choing, S. N.; Aschaffenburg, D. J.; Pemmaraju, C. D.; Prendergast, D.; Cuk, T. The formation time of Ti-O• and Ti-O•- Ti radicals at the n-SrTiO3/aqueous interface during photocatalytic water oxidation. *J. Am. Chem. Soc.* 2017, *139*, 1830−1841.
(47) Herlihy, D. M.; Waegele, M. M.; Chen, X.; Pemmaraju, C. D.; Prendergast, D.; Cuk, T. Detecting the oxyl radical of photocatalytic water oxidation at an n-SrTiO3/aqueous interface through its subsurface vibration. *Nat. Chem.* 2016, *8*, 549−555.
(48) Goryachev, A.; Etzi Coller Pascuzzi, M.; Carla, F.; Weber, T.; Over, H.; Hensen, E. J. M.; Hofmann, J. P. Electrochemical stability of RuO2(110)/Ru(0001) model electrodes in the oxygen and chlorine evolution reactions. *Electrochim. Acta* 2020, *336*, No. 135713.
(49) Nandjou, F.; Haussener, S. Modeling the Photostability of Solar Water-Splitting Devices and Stabilization Strategies. *ACS Appl. Mater. Interfaces* 2022, *14*, 43095−43108.